Ultrasonics Sonochemistry 119 (2025) 107404

Contents lists available at ScienceDirect

Ultrasonics Sonochemistry

journal homepage: www.elsevier.com/locate/ultson

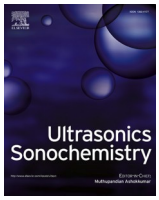

Reconfigurable acoustic streaming tweezers enabled portable liquid handler for nucleic acid extraction

Tiechuan Li [1], Rui You [1], Xiaotian Shen, Zhiwei Li, Yang Yang, Ziyu Han, Xuexin Duan [*]

State Key Laboratory of Precision Measuring Technology & Instruments, Tianjin University, Tianjin 300072, China

ARTICLE INFO

Keywords:
Extraction
Microfluidics
Numerical simulations
Acoustic streaming
Nucleic acids

ABSTRACT

The extraction and purification of nucleic acids (NA) play a crucial role in biomedicine, as high-purity and efficient extraction are essential prerequisites for accurate molecular diagnosis. Consequently, beads clumping and complex peripherals hinder the development of portable NA extraction apparatus. In this study, a novel reconfigurable acoustic streaming tweezer (RAST) is proposed. Two MEMS fabricated solid-mounted thin-film piezoelectric resonators (SMRs) are integrated into a compact reaction chamber. The high-frequency (>1 GHz) acoustic wave induces fast liquid flow and particle movement through the Stokes drag. By carefully designing the structure of the device and the operation program, the RAST can be switched between the chip-based centrifuge-type particle separation and the vortex-type solution mixing modes, enabling automated NA extraction without complex peripherals. Numerical simulations and micro particle image velocimetry (PIV) experiments are conducted to thoroughly investigate the particle manipulations and mixing conditions in the double SMR mode (D-SMR) and the single SMR mode (S-SMR). A portable liquid handler based on the RAST is designed and applied to NA extraction from different samples (buffers, serum, and whole blood). After optimization, the system achieves an 80 % NA recovery rate from rat whole blood. Combined with real-time quantitative PCR, the detection sensitivity for adenovirus (DNA) and COVID-19 (RNA) is as low as 10^2 IU/mL. When handling samples smaller than 200 μL, the sensitivity is more than 1.56 times higher than that of commercial automated liquid handling systems.

1. Introduction

Polymerase chain reaction (PCR) based specific nucleic acids (NA) analysis, also known as molecular tests, has been widely used for forensic, environmental, and clinical applications including DNA fingerprinting, detecting bacteria or viruses, and diagnosing genetic disorders [1]. It has gained more attentions since the outbreaks of COVID-19 pandemic as the nose or mouth swab PCR test is an accurate and reliable way for diagnosing COVID-19 [2]. However, conventional PCR is processed in laboratories, which largely delay the detection results. Current trend is developing miniaturized and automatic PCR test to facilitate on site point-of-need testing (PONT). Lee et al. reported an innovative polymer lab-on-a-chip (LOC) for reverse transcription (RT)-PCR, which can be used for the analysis of human immunodeficiency virus (HIV) with the on-chip RT-PCR and chemiluminescence assays in shorter than one hour with minimized cross-contamination [3]. Wu et al. reported the construction of a polymerase chain reaction (PCR) device for fast amplification and detection of DNA. The DNA amplification happens on an interchangeable chip with the volumes as low as 1.25 μL, while the heating and cooling rate was as fast as 12.7 °C/s ensuring that the total time needed of only 25 min to complete the 35 cycles PCR amplification [4]. In response to the need for rapid and varied disease detection, Lee et al. developed a multiplex real-time RT-PCR (rRT-PCR) assay for the detection of influenza A and B viruses, parainfluenza viruses 1–4 (PIV1-4), human metapneumovirus, adenovirus, human rhinovirus, respiratory syncytial virus (RSV), and SARS-CoV-2 [5].

In a regular PCR test, NA extraction and enzymatic amplification are the two major steps. Sufficient extraction and purification of NA is rather essential especially in PONT, since contaminants from the complex matrices often inhibit enzymatic amplification, which will result in poor reproducibility and low sensitivity. Despite the great efforts have been made for miniaturizing amplification apparatus, the portable extraction setup has been less developed [6]. Shrinking the size of the NA

* Corresponding author.
E-mail address: xduan@tju.edu.cn (X. Duan).
[1] These authors contributed equally to this work.

https://doi.org/10.1016/j.ultsonch.2025.107404
Received 31 December 2024; Received in revised form 9 February 2025; Accepted 27 May 2025
Available online 29 May 2025

extraction setup is challenging since numerous sample handling steps are generally required [7]. For example, in a typical solid phase NA extraction approach, which normally includes (i) cell lysis, (ii) NA binding, (iii) washing and, (iv) elution. For all these steps, mixing of the reaction, beads incubation, washing, and separation are required to perform the full extraction. This poses a high difficulty in miniaturization of the extraction instrument.

Microfluidic systems have been developed as alternative NA extraction tool by reducing the sample volumes, which is compatible for PONT requirement. For example, magnetic and spin column assisted on-chip NA extraction are most common approaches adapted on chip [7]. A microchip based on solid phase extraction (SPE) method has been established for the purification of RNA from biological samples [8]. Early versions of microfluidic-based NA extraction devices required up to multiple actuators or external pumping devices for fluid manipulation and valve control [9,10]. However, the utilization of external equipment increased the size and cost of the device, despite achieving automated extraction [11,12]. Additionally, the contact between external equipment and internal chips heightened the risk of cross-contamination [13]. Similarly, pneumatic-driven devices encountered comparable challenges [14,15]. Methods utilizing pre-set vacuum for liquid transfer and fluid manipulation circumvent the need for external equipment, but their applicability is limited to low throughputs. Zhang et al. demonstrated a microfluidic chip for DNA extraction using the solid-phase extraction method. They showed that with this chip and HindIII-digested k-phage DNA as the sample, DNA extraction could be completed within 15 min, however, the efficiency was only approximately 50 % [16]. The low throughput of the microfluidic system hinders their real applications, which is typically limited to below 100 μL. Additionally, the less efficient mixing conditions in such low Reynolds number systems often result in aggregations of the magnetic beads, limiting the extraction efficiency and the total amount of extracted NA, which inevitably leads to low sensitivities and false negatives. An ideal portable NA extraction system is a handheld-sized device capable of achieving high NA extraction yields from complex matrices, adaptable to different amounts of input samples, minimizing the amount of co-extracted impurities with NAs, reducing operation times, and compatible with different chemicals and solid sorbents.

In this work, we propose a novel reconfigurable acoustic streaming tweezer (RAST), where two MEMS fabricated solid-mounted thin-film piezoelectric resonators (SMRs) are integrated into a compact reaction chamber (Fig. 1). The high frequency acoustic wave induces fast liquid flow and particles movement by the Stokes drag. By dedicatedly designing the structure of the apparatus and the operation program, the RAST can be switched between centrifuge type particles separation and the vortex type solution mixing model. Such reconfigurable operations enable the automated NA extraction without using complicated peripherals. We thoroughly investigated the particles manipulations and mixing conditions in the double SMRs mode (D-SMR) and the single SMR mode (S-SMR) through numerical simulations and micro particle image velocity (PIV) experiments. We further designed a portable liquid handler based on the RAST and applied for NA extraction from different samples (buffers, serum and whole blood). The compact size of the apparatus and the low power consumption largely facilitates the on-site NA extraction that overcomes the aforementioned limitation. After dedicate optimization of the particles manipulations and mixing conditions, the proposed robotic liquid handling system reaches 80 % NA recovery from rat whole blood. By combining with real-time qPCR, it demonstrates for DNA (adenovirus) and RNA (COVID-19) based virus detection as low as 10^2 IU/mL. Especially, it shows more than 1.56 times increased in sensitivity when handling sub-200 μL samples, compared with commercial automated sample handling system.

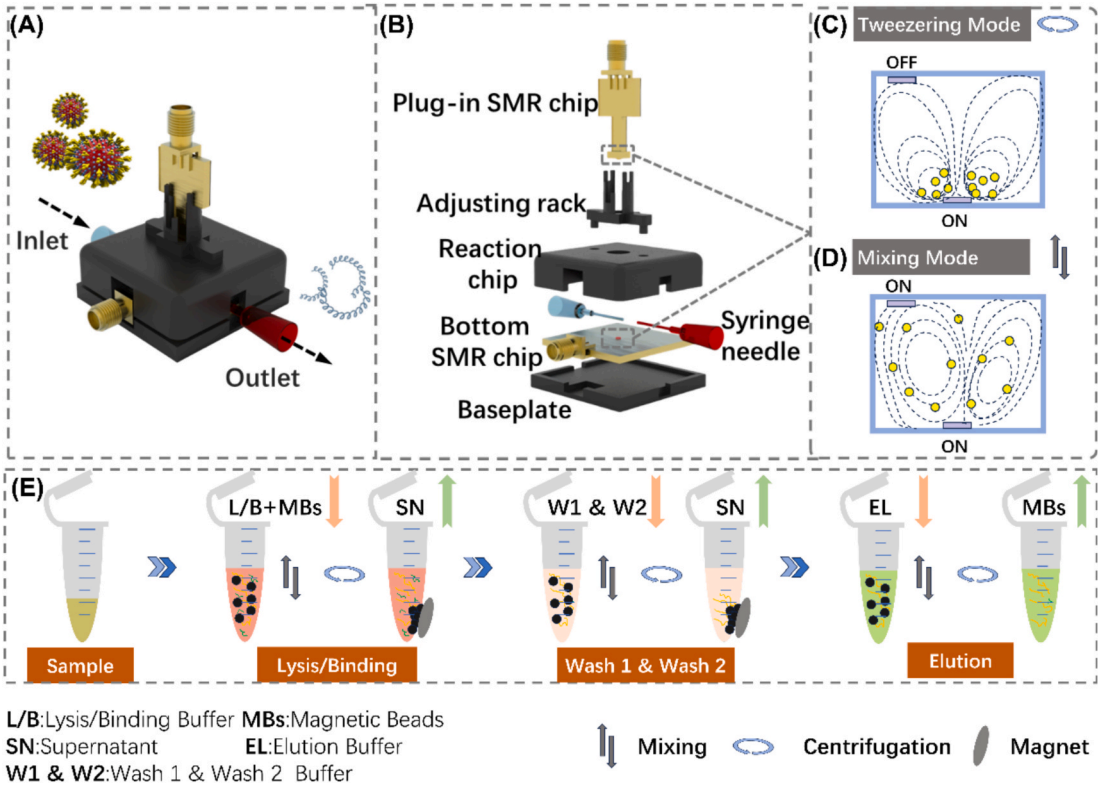

Fig. 1. (A) Schematic of the acoustic extraction module; (B) The exploded view of the acoustofluidics module (C)Tweezering mode; (D) Mixing mode; (E) Manual workflow.

2. Materials and method

2.1. Reagents and NA extraction

2.1.1. Total genomic DNA extraction from whole blood

Whole blood samples were collected from SD rats (Tianjin YiShengYuan Bio. Technology Co. LTD, China) into vacutainer tubes (BD Vacutainer) containing ethylenediaminetetraacetic acid to prevent coagulation. A whole blood genomic DNA extraction kit (Genmag Bio. Technology Co. LTD, China, cat. NA001-1) was employed, following the manufacturer's protocol as outlined in Table S1. The concentration of the target DNA was measured using the NanoDrop 2000 Spectrophotometer (Thermo Fisher, Waltham, MA). Prior to the experiments, devices and tubes were coated with a 2 % bovine serum albumin solution (Tianhang Bio. Technology Co. LTD, China, cat. 22012–8612) in 1 × PBS (pH 7.4, Solarbio Life Sciences) for five minutes at room temperature to prevent nonspecific adsorption of NA fragments. Subsequently, the system was rinsed with nuclease-free water (QIAGEN) and allowed to dry for several minutes before proceeding with the experiments. In the nucleic acid extraction experiment, 5 mL of whole blood from mice was used. The nucleic acid recovery rate was calculated by dividing the actual amount of nucleic acid extracted by the maximum amount of nucleic acid that can be extracted as specified by the commercial kit, and the final recovery rate reached 80 %.

2.1.2. Adenovirus (ADV) DNA extraction from bovine serum

Spiked ADV (Hanheng Bio. Technology Co. LTD, China, cat. HB-AP2100001) was dissolved in bovine serum at concentrations ranging from 10^1 to 10^6 IU/mL. A virus DNA/RNA extraction kit (Genmag Bio. Technology Co. LTD, China, cat. NA007-1) was used for ADV DNA extraction, following the manufacturer's protocol provided in Table S2.

2.1.3. COVID-19 RNA extraction from Phosphate Buffer Saline (PBS) solution

Spiked COVID-19 virus (Fubaiao Bio. Technology Co. LTD, China, cat. FNV2001) was dissolved in 1 × PBS at concentrations ranging from 10^3 to 10^6 copies/mL. A virus DNA/RNA extraction kit (Genmag Bio. Technology Co. LTD, China, cat. NA007-1) was utilized for COVID-19 RNA extraction, following the manufacturer's protocol detailed in Table S3.

2.2. Real-time qPCR

In this study, two types of NAs require amplification and detection. The SLAN-96P Real-Time PCR System, acquired from Shanghai Hongshi Medical Technology Co., Ltd., China, was used for these detections. A NA detection kit from Takara Bio Inc. (Product code: R007Z, Japan) was employed for the PCR detection of adenovirus (ADV). Sequences for the primers and probe used were as follows: forward primer (ADV-F) 5′-TGC TGC CCG ACA ACC ATC-3′, reverse primer (ADV-R) 5′-TCA CGA ACT CCA GCA GGA CCA-3′, and probe (ADV-P) 5′-TGA GCA CCC AGT CCG CCC TGA GCA-3′ (Sangon Biotech (Shanghai) Co., Ltd., China). PCR cycles to obtain amplicons included an initial denaturation at 95 °C for 3 min, followed by 40 cycles: 95 °C for 3 min, 95 °C for 10 s, and 60 °C for 30 s. The final PCR volume of 25 μL comprised 2.5 μL 10 × Buffer, 2 μL dNTP, 0.2 μL DNA polymerase, 0.5 μL each of ADV-F, ADV-R, and ADV-P, 13.8 μL of DI water, and 5 μL of eluted DNA sample.

The TaKaRa Taq™ Hot Start Version kit (Product code: PR064A, Japan) from Takara Bio Inc. was utilized for the RT-PCR detection of COVID-19 RNA. The sequence for the forward primer was 5′- CCC TGT GGG TTT TAC ACT TAA −3′, that for the reverse primer was 5′- ACG ATT GTG CAT CAG CTGA −3′, and that for the probe was 5′- CCG TCT GCG GTA TGT GGA AAG GTT ATGG −3′ (Sangon Biotech (Shanghai) Co., Ltd., China). PCR cycles to achieve amplicons started with 42 °C for 5 min and 95 °C for 10 s, followed by 40 cycles: 95 °C for 5 s and 56 °C for 45 s. The final PCR volume of 20 μL included 10 μL 2 × Buffer, 0.4 μL RT Enzyme, 0.4 μL DNA polymerase, 0.8 μL each of forward primer, reverse primer, and probe, 2.8 μL of nuclease-free water, and 4 μL of eluted DNA sample.

2.3. Image acquisition and analysis

Data for the acoustofluidic field characterization experiments were collected using a commercial micro PIV system (LaVision, Germany). This system includes a long-distance microscope (12X), a double-pulsed 532 nm Nd-YAG laser, a programmable timing unit (PTU), a CMOS camera, and Davis 8.3 software. Images and videos were captured using an Olympus BX53 optical fluorescence microscope (Japan).

3. Results and discussion

3.1. System design and integration

As shown in Fig. 1, the RAST composes of two SMRs integrated in a compact reaction chamber, which allows for handling sample volumes ranging from 10 to 400 μL. The two gigahertz (GHz) SMR devices were positioned at the top and bottom of the extraction chamber, which contact directly to the solution and can be electrically addressed separately. Fig. 1(B) depicts an exploded view of the system. The reaction chamber contains a 'step rack' structure so that the spacing between the two SMRs could be adjusted to meet the NA extraction needs for different sample volumes. The SMR, shown in Fig. S1, is a pentagonal bulk acoustic wave resonator operating at 2.5 GHz, constructed using a sandwich piezoelectric structure with an underlying Bragg reflector, fabricated via standard microelectromechanical systems (MEMS) technology. The fabrication details of the device have been reported in our previous publication [17]. The real pictures of the various parts are shown in Fig. S2, where the whole apparatus is comparable in size to a coin, highlighting its portability and integration.

For miniaturization of the system, we customized a signal generator and a power amplifier in a PCB board and assembled it into the RAST system (Fig. S3). The duration and power amplitude of the acoustic waves could be conveniently controlled and adjusted using the programmed signal generator. Two syringe needles were used as liquid connections, which work as the input of samples and reagents, as well as the output of waste liquid and NA products. The whole liquid handler is 40 mm × 40 mm × 40 mm in size, less than 30 g in weight, which is rather suitable for portable applications.

A single SMR has been demonstrated as acoustic streaming tweezers (AST) for microbeads (MBs) trapping due to the combination of the acoustic radiation force (ARF) and the acoustic streaming (drag) force (ASF) induced by the high-speed acoustic streaming flow [18,19] (Fig. 1(C)). Here, the innovative double SMR configuration enables the switches between particles trapping and solution mixing. Such (RAST) facilitates multi-steps of liquid handling without complicated peripheries (Fig. 1(D)).

The NA extraction process is based on well-established Solid Phase Extraction (SPE) approach, which generally involves binding of DNA to a solid support (i.e., MB), followed by washing and elution of the DNA from the MBs. Reaction to bind the DNA and centrifugation to separate the bound DNA from other cellular components are generally required using multi-steps of liquid handling and particles operations (Fig. 1(E)). We designed the RAST operating in two basic modes: 1) a single SMR operating at tweezering mode, which traps and separates MBs from the waste liquid, functioning as a chip-based centrifuge (Fig. 1(C)); 2) two SMRs operating at mixing mode, which mixes the MBs with the solution, acting as a miniaturized vortex mixer (Fig. 1(D)). Programmed switching between these two modes enables the automated NA extraction including the sample lysis, NA binding, MBs separation, washing, NA elution, etc.

3.2. Tweezering mode

As can be seen from Fig. 1(E), multiple centrifugations are used to reduce the loss of NA adhering to the wall of Eppendorf tube. However, centrifugation operations can lead to problems such as increased size of peripheral devices and contamination caused by opening the lids. Our tweezer system solves this problem. The D-SMR system achieves a closed condition for the system, and the design of the entrance and exit eliminates the need for opening the lid. Moreover, the entire device is palm-sized.

The ARF and ASF play significant roles in acoustic manipulation techniques, particularly in contexts involving standing surface acoustic waves (SSAW) and acoustic streaming induced by oscillating microbubbles [20] or microstructures [21]. For MBs larger than the acoustic length in this work, the ARF and ASF can be given by

$$\boldsymbol{F_{ASF}} = 6\pi\mu a(\boldsymbol{v} - \boldsymbol{v_p}) \tag{1}$$

$$F_{ARF} = B\frac{\pi(2p_1)^2a^2}{\rho_0 c_0^2} \tag{2}$$

where μ represents viscosity, a denotes MB radius, v signifies fluid velocity, v_p is MB velocity, B is an adjustable constant, p_1 represents the acoustic pressure,ρ_0 is the medium's density, and c_0 denotes the acoustic velocity in the medium. According to Eq. 1–2, Fig. 2(A) illustrates how the ASF (blue arrows) pulls MBs moving along the vortices, while the ARF (red arrows) drives MBs along the acoustic pressure gradient and toward the vortex centers. As shown in Fig. 2(B-D), the fluid velocity decreases toward the vortex center, and the acoustic pressure sharply declines along the acoustic wave propagation direction. As a result, the ARF gradually diminishes to a critical point, where it no longer propels MBs toward the vortex center, and MBs move in current tracks together with the ASF, thereby facilitating MB manipulation. Through tuning the applied power to adjust the critical point, the stable tracks of MBs can be changed to provide different functions, such as capture in a small region (low power) and mix in the whole region (high power) (Fig. 2(B)).

MBs capture were comprehensively simulated and discussed using a three-dimensional (3D) high-frequency traveling bulk acoustic wave fluidic model through finite element method (FEM) in previous work [18]. According to the theory mentioned above, 5 μm polystyrene (PS) MBs (similar to those used in magnetic beads from NA extraction kits) were consistently captured by the SMR. As illustrated in Fig. 2(C), the effective operating distance of the acoustic pressure is below 50 μm, which is approximately 10 times the size of MBs. Given that the resonance area is 20,000 μm^2, under ideal conditions, the surface of the device can accommodate approximately 1,000 MBs, and multiple layers can capture up to 10,000 MBs. This capacity matches the total number of MBs in a reagent kit, meaning that there are sufficient binding sites to capture varying quantities of nucleic acids (commercial reagent kits typically have MBs with binding sites that are excessively numerous to cover the total amount of nucleic acids from multiple samples). Fig. 2(E) depicts the MBs capture experiment. Over time, an increasing number of MBs were trapped around the device. Video S1 shows the MBs capture process, with an input power of 5.4mW. Therefore, a single SMR operating at low power can effectively trap MBs, functioning akin to a miniaturized on-chip centrifuge.

The multiphysics software, COMSOL 6.0, was utilized to elucidate the principles underlying MB capture and separation. Based on prior research [19], coupling the solid mechanics, electrostatics, pressure acoustics, and laminar modules in COMSOL 6.0 allows us to study the acoustic streaming field distribution, as depicted in Fig. 2(D). The SMR is positioned at the bottom center of a chamber (6 mm in width and 5 mm in height). Power inputs of 5.4 mW and 200 mW were applied to the SMR, respectively. Owing to the symmetric morphology of the vortex on the SMR, we selected one vortex for detailed study and juxtaposed the flow field diagrams under both power conditions for clear comparison.

In the system, when the power is set as 5.4 mW, the acoustic vortex center is close to the SMR surface, and the ARF and the ASF together drag the MBs into the track close to vortex center, eventually achieving the stable capture to MBs. While as the power increases to 200 mW, the vortex center is about 2.5 mm away from the SMR in longitude, which is much larger than the effective range of action of the ARF (previous works [17,18,22] proved that this action range under GHz acoustic wave is lower than 50 μm). Obviously, in such condition where the ASF acts as

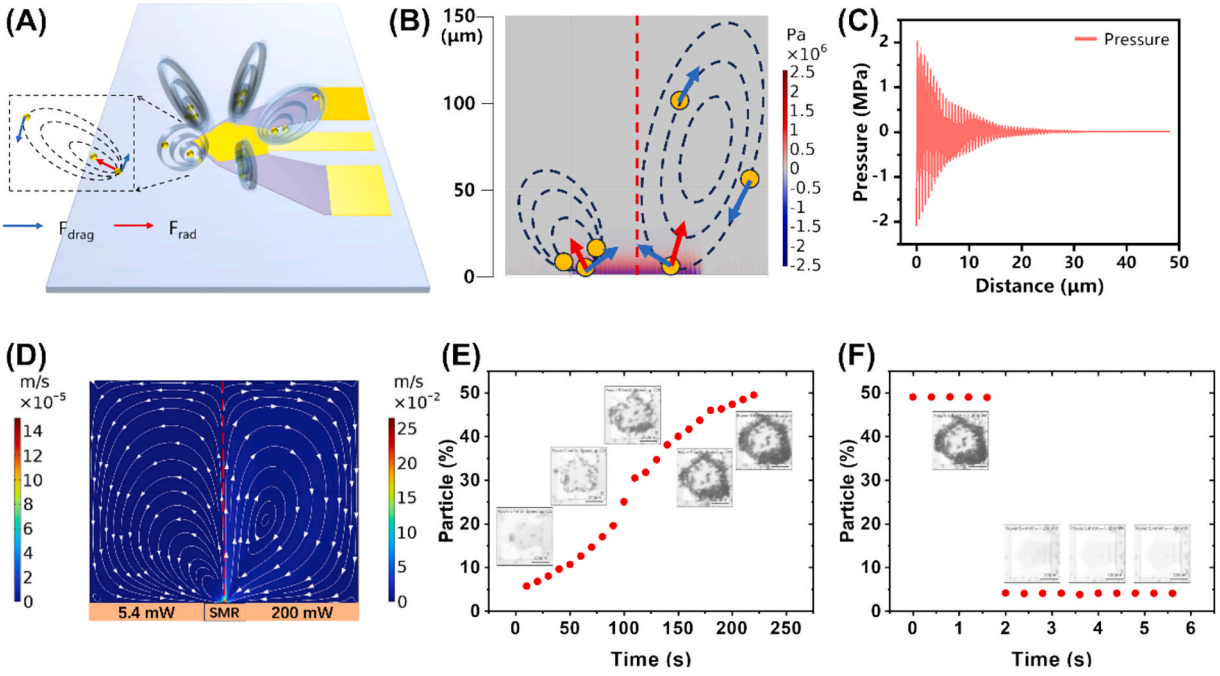

Fig. 2. (A) Force analysis diagram of MBs over the SMR; (B) Force analysis under different powers (5.4 mW and 200 mW); (C) The acoustic pressure distribution along the propagation direction (red dashed line in (B)); (D) The flow field distribution under 5.4 mW and 200 mW power input; (E) MB capture; (F) MB separation. (For interpretation of the references to colour in this figure legend, the reader is referred to the web version of this article.)

the main action force, the MBs are mixed in space. Thus, the MBs capture and mixing can be freely switched by adjusting the input power, as shown in Video S1 and S2. As shown in Fig. 2, it can be found that with the power increasing, the flow velocity also increases, which is corresponding to Fig. S4 (A). To demonstrate the ability of the acoustic streaming tweezer (AST) to induce strong flow field, a high-speed camera (Photron UX50, Japan) was employed to capture MB trajectories under a microscope at a frame rate of 10,000 frames per second (fps). To measure the fluid velocity in the acoustic streaming, a PIV system assisted by hollow glass MBs was used to trace the streaming effect, as shown in Fig. S4(A). Interestingly, when the input power exceeds 300 mW, the MB velocity shows a linear relationship with the input power. Additionally, microscale solid-phase carriers in liquid achieve an instantaneous velocity of 300 mm/s in sample volumes of hundreds of microliters.

When the power is less than 5.4 mW, the height of the vortex center is almost below 50 μm. However, when the power increases to 10 mW, the height of the vortex center exceeds 50 μm. At this time, the MBs mostly exist in a spatially dispersed form, with ASF being dominant and ARF being negligible. Therefore, 5.4 mW was chosen for MB capture. When the power increases to 200 mW, the height of the vortex center reaches 2.5 mm, and the effective vortex field covers the entire flow field. As the power continues increasing, the vortex height also continues increasing. However, secondary vortices will be generated, and higher power leads to greater energy consumption. Therefore, 200 mW is the preferred power for MB spatial mixing (the detailed data can be found in Fig. S4 (B)). It is worth noting that when dealing with complex samples, such as whole blood, placing two SMR devices opposite each other can achieve a better mixing effect. A detailed explanation will be elaborated in the following text.

3.3. Mixing mode

NA extraction methods using silica magnetic MBs offer several advantages, including ease of execution, automation, high throughput, and high sample processivity [7]. However, magnetic MBs tend to aggregate after being exposed to a strong magnetic field. Moreover, these clusters result in heterogeneity and reduce the surface area available for capturing NAs. Finally, the target analyte is in very low concentrations [23].

In addressing this issue, the acoustic mixing methods have been developed as illustrated in Table 1, which facilitate the enhancement of mass transfer efficiency of the target analyte via effective convection processes:

$$\frac{\partial c}{\partial t} = \nabla \bullet (D\nabla c) - \boldsymbol{v} \bullet \nabla c \tag{3}$$

where c is the of analytes, and D is the molecular diffusion coefficient. In 2016, Ida Iranmanesh et al. extensively analysed the advantages and disadvantages of acoustic mixers in processing biological samples [24]. Although acoustic mixers enable high-efficiency mixing, they also generate significant heat, thereby necessitating cooling devices. To maintain effective mixing while reducing power consumption, acoustic mixers utilizing bubbles were proposed [23,25]. However, bubble-based micromixers suffer from several limitations, including bubble instability, heat generation, and challenges in bubble trapping processes [26]. To address these challenges, Tony Jun Huang and collaborators developed oscillating sharp-edge-based micromixers that utilize acoustically generated microvortices, akin to bubble-based micromixers, yet with the added benefits of convenience and stability [26,27]. Additional acoustic mixing devices employing chip-structured auxiliaries include vibrating membranes with holes [28] and cilia oscillation [29]. However, both bubble auxiliaries and chip-structured auxiliaries increase the complexity of chip processing and fluidic channel resistance. Moreover, acoustic streaming-based mixing is mostly applied in microfluidic

Table 1
Acoustic mixing devices.

Reference	Material	Operation frequency (Hz)	Bubble auxiliary	Structure auxiliary
Alvaro J. Conde *et al.* [23]	lead zirconate titanate piezoelectric ceramics (PZT)	4.2 k	yes	Channel with air pockets
Robin H. Liu *et al.* [25]	lead zirconate titanate piezoelectric ceramics (PZT)	5 k	yes	Channel with air pockets
Po-Hsun Huang *et al.* [26]	lead zirconate titanate piezoelectric ceramics (PZT)	4.5 k	no	Oscillating sidewall sharp-edges
Hunter Bachman *et al.* [27]	lead zirconate titanate piezoelectric ceramics (PZT)	4.9 k	no	Oscillating sidewall sharp-edges
Hoang Van Phan *et al.* [28]	silicon nitride	more than 100 k	no	Vibrating membrane with holes
Sinem Orbay *et al.* [29]	lead zirconate titanate piezoelectric ceramics (PZT)	4.6 k	no	Cilia oscillation
This work	aluminum nitride (AlN)	2.5G	no	no

systems, and the sample volume processed in a single chamber is usually below hundreds of microliters. Therefore, a nucleic acid extraction technique for milliliter or even sub-milliliter samples urgently needs to be proposed. Our group developed an acoustofluidic chip utilizing a GHz SMR, capable of straightforward insertion into microchannels [30] or chambers [31] to produce robust microvortices without relying on bubbles or chip structures. Furthermore, the excellent biocompatibility of our acoustic devices has been demonstrated [32,33]. Therefore, the GHz SMR-induced acoustic streaming may be a desirable counterpart to provide efficient mixing.

The mixing index (M) serves as a dimensionless metric to quantify the uniformity of substance concentration, thereby indicating the efficiency of flow field mixing [34]:

$$M = \left(1 - \sqrt{\frac{1}{N}\sum_{i=1}^{N}\left(\frac{c_i - \bar{c}}{\bar{c}}\right)^2}\right) \times 100\% \tag{4}$$

where N is the total number of sampling points, c_i and $\bar{c}$ are normalized concentration and expected normalized concentration, respectively. When M equals 0 %, it indicates the absence of mixing; whereas, when M reaches 100 %, it signifies a complete mixture.

To optimize the mixing efficiency, we conducted a simulation study on the AST induced by the SMR (Fig. 3). The control equations (Navier-Stokes equation, body force formulation, etc.) and detailed simulations are elaborated upon in the supplementary information (SI). Fig. 3 shows the mixing index when each device has been activated for three seconds. Analyzing the acoustic streaming field under identical boundary conditions, the mixing indexes of the D-SMRs (with placement angles of 11° and 22°) are markedly enhanced compared to that of the S-SMR (Fig. 3 (H)), highlighting the significant role of vortex interaction. Focusing on the placement angles of the D-SMRs, it is evident that variations in these angles elicit alterations in the vortex flow patterns. When the SMRs are aligned in direct opposition, the mixing efficiency suffers from the mutual restraint of vortices generated by each device, thereby confining

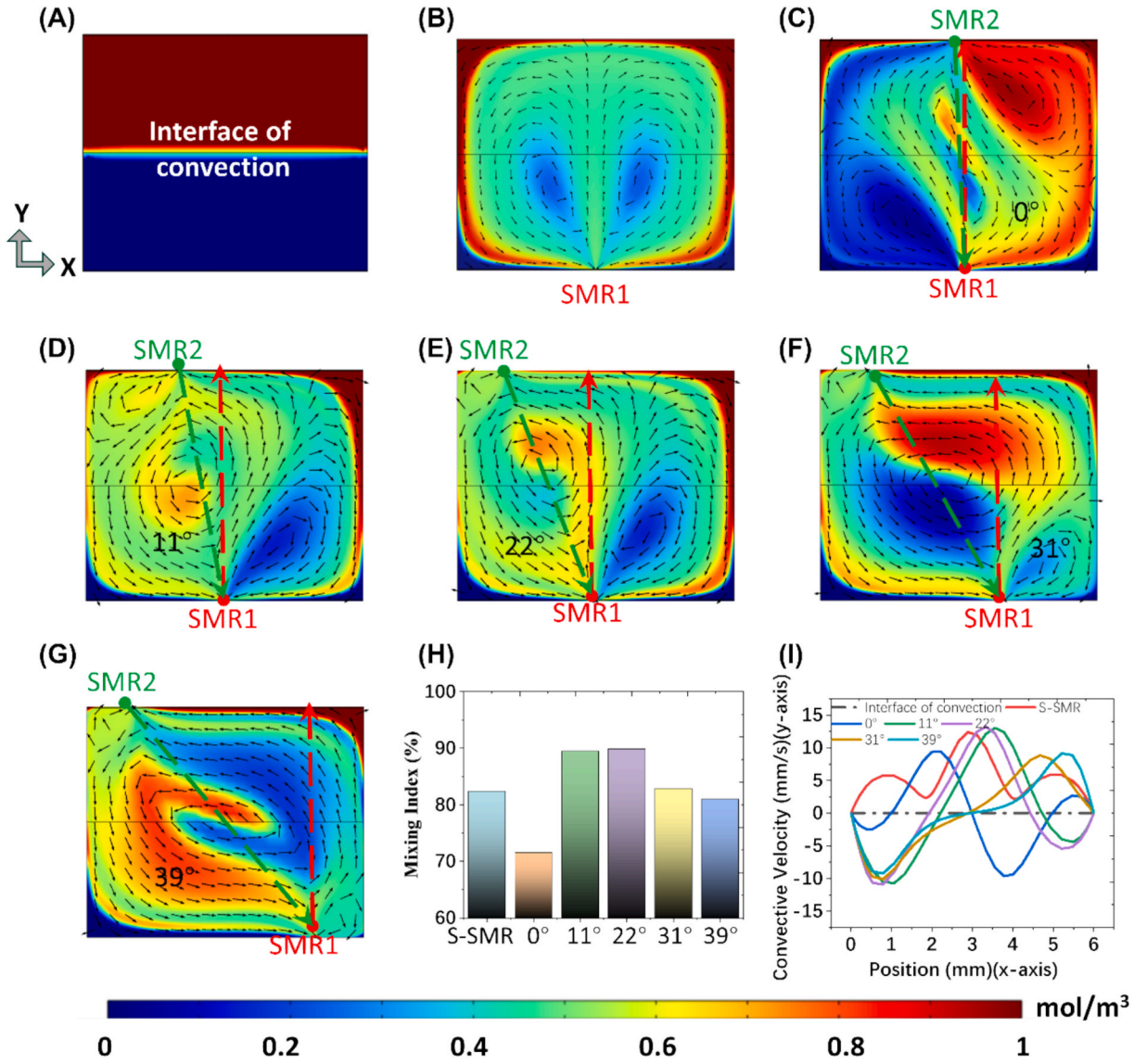

Fig. 3. The mixing performance of SMR-induced AST. (A) Original state; (B) S-SMR system; (C-G) D-SMR systems with different placement angles (indicated by the green and red dashed lines); Mixing indexes (H) and convective velocity distributions (I) of S-SMR system and D-SMR systems at 3 s. (For interpretation of the references to colour in this figure legend, the reader is referred to the web version of this article.)

mixing within their individual domains. By increasing the lateral distance between the devices to enlarge the placement angle, there is adequate space for vortices interaction, thereby increasing mixing efficiency. As the placement angle continue increasing to 30°, the interaction between the vortices of the double SMRs weakens in such large space, resulting in a superposition of the SMRs and a lower mixing index compared to those at placement angles between 11° and 22°. Upon further investigation, it can be observed that, when the placement angle is set between 11° and 22°, the convective velocity at the interface of the two-phase solution becomes the strongest. In the S-SMR convective mode, the fluid in the lower layer (represented by blue) impacts the fluid in the upper layer (represented by red), and the mixing index is lower than that of the D-SMR non-inhibitory mode (with placement angle ranging from 11° to 22°). And this would be further proved by the performance of the two modes in the extraction of nucleic acids from whole blood in the following study.

Once the placement angle of the SMRs is optimized, we proceed to define the boundary dimensions of the chamber. With a constant sample volume of 142 μL, the cross sections of the cylindrical chamber are set as 6000 × 5000 μm^2, 8000 × 2812.5 μm^2, and 10000 × 1800 μm^2, respectively. Fig. 4 demonstrates that, at a placement angle of 22°, the mixing index peaks in a chamber with 6000 μm in diameter and 5000 μm in height. Reducing the chamber height and increasing the diameter compress the vortices, resulting in a reduced exposure to strong vortices and a decrease in the mixing index.

3.4. NA extraction from multiple samples

Based on the above analyses, MB capture, separation and mixture can be achieved by reconfiguring the AST. Consequently, a portable and miniaturized NA extraction system can be developed based on the RAST (Fig. 1(A)). To verify the biochemical application capabilities of the system, we extracted NAs from three different samples. The extraction of nucleic acids from the whole blood sample poses a challenge to the NA extraction system due to the complexity of the biological substances in the whole blood. Given the complexity of substances in whole blood samples, we employed the RAST system operating at S-SMR/D-SMR in NA extraction. In order to compare the NA extraction performances of

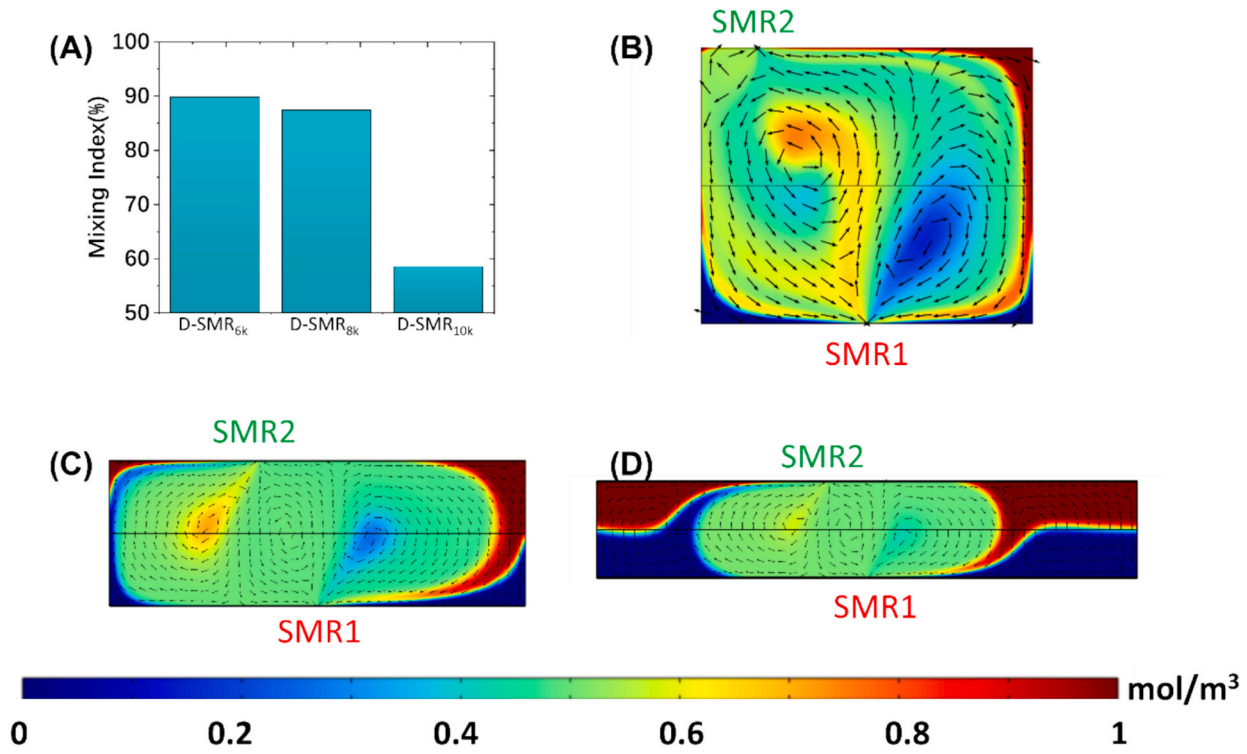

Fig. 4. The mixing performances of D-SMRs with different boundary dimensions.

the two systems, we tested the concentration of NA extracted from different volumes of whole blood samples. As depicted in Fig. 5(D), the D-SMR, with two SMRs positioned in a complementary configuration, exhibits significant advantages in NA extraction from various sample volumes compared to the S-SMR. To ensure experimental comparability and consistency, the SMRs were operated at an input power of 200 mW,

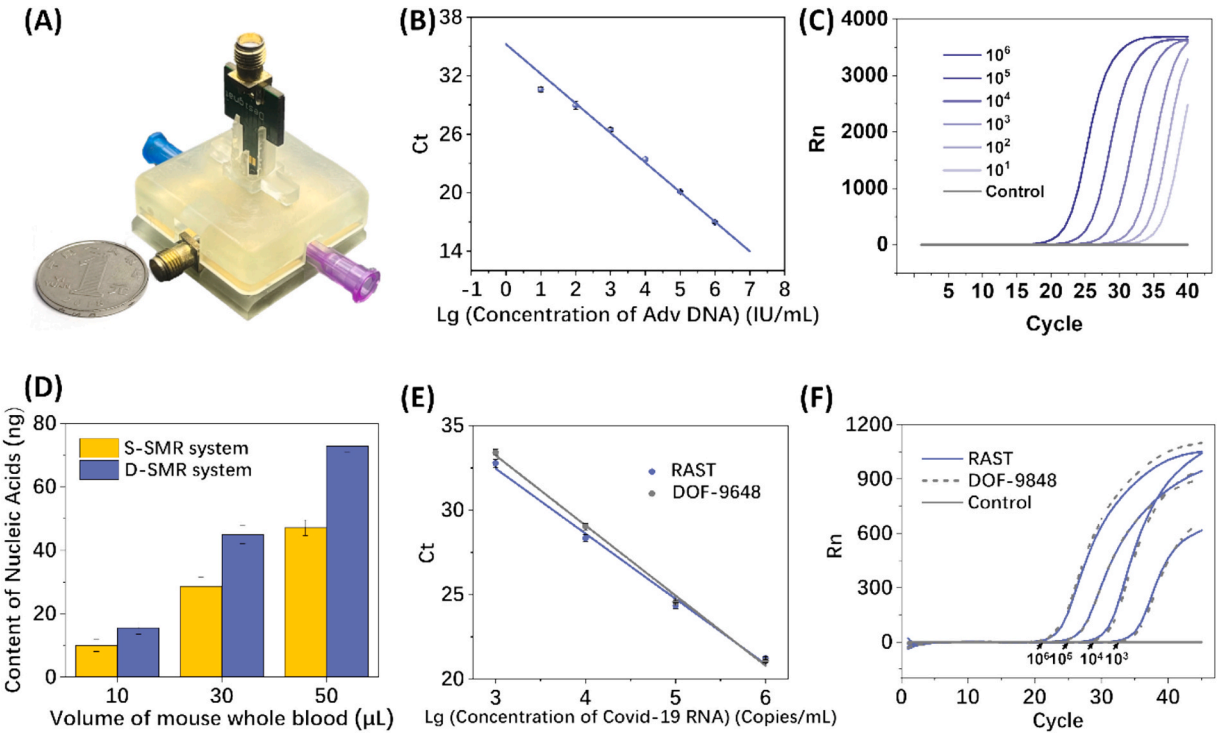

Fig. 5. (A) The photograph of RAST system; (B) Linear relationship between the cycle threshold (Ct) value of PCR and the concentration of ADV DNA using the proposed method; (C) PCR curves for the detection of ADV DNA at different concentrations ranging from 10 IU/mL to 10^6 IU/mL; (D) The DNA extraction content with different volume of mouse whole blood at different modes; (E) Linear relationship between the Ct value of PCR and the concentration of COVID-19 RNA using the RAST and the commercial NA extractor; (F) PCR curves for the detection of COVID-19 RNA at different concentrations ranging from 10^3 Copies/mL to 10^6 Copies/mL using the RAST and the commercial NA extractor.

and with sample volumes of 10 μL, 30 μL and 50 μL, respectively (Table S1). Obviously, the D-SMR provides a better extraction performance than the S-SMR, which can be attributed to the following two reasons. Firstly, the D-SMR exhibits a stronger vortex effect compared to the S-SMR, resulting in a higher concentration of extracted material. Fig. 3 illustrates the scenario where only the bottom SMR is activated at 200 mW input power, showing two vortices visible in the side view of the system. Activating the upper SMR (200 mW) results in the formation of multiple vortices in the space. An opposite position increase the spatial interaction area of the vortices, intensifying mixing. Secondly, the whole blood contains numerous impurities, which may adhere to the SMR surface to reduce the vibrational capacity. At D-SMR, the two SMRs positioned opposite each other allow for the mutual cleaning, i.e., one device removes residual MBs from the surface of the other device, thereby maintaining both devices in optimal condition. Therefore, owing to the strong mixing effect of the D-SMR, its DNA recovery rate can reach approximately 80 % (50 μL), whereas that of the S-SMR is only about 50 %. This result also validates the simulation results in Fig. 3, albeit with the caveat that whole blood samples used in the actual experiment contain more complex components.

The free adenovirus (ADV) DNA in plasma and the SARS-CoV-2 RNA in throat swabs are both low-concentration NAs. Therefore, the challenge in their extraction lies in achieving a high recovery rate of nucleic acids from a small number of samples. Meanwhile, the extraction of free nucleic acids by the magnetic bead method also has the problem that serious aggregation after magnetic bead adsorption significantly affects the NA binding sites [23]. Through the RAST system working at D-SMR, we carried out the extraction of these two types of low-concentration nucleic acids. Building on the successful mouse whole genome extraction, the RAST extraction system was applied to extract ADV DNA from bovine serum. Fig. 5(B&C) display the results of ADV DNA extraction from bovine serum. A strong linear calibration curve of the Ct value of PCR and the concentration (C) of ADV DNA was obtained, and described by $Ct = -3.035\log(C) + 35.322$ ($R^2 > 0.99$). The ADV samples of known concentrations (ranging from 10 IU/mL to 10^6 IU/mL) were used, confirming valid Ct values for concentrations from 10^2 IU/mL to 10^6 IU/mL and invalid for 10 IU/mL (see Table S2 for experimental details). Thus, the limit of detection (LOD) of this method is established at 10^2 IU/mL. This LOD is highly compatible with current commercial instruments. Fig. 5(E&F) display the results of COVID-19 RNA extraction using the RAST system and the DOF-9648 commercial NA extractor (Genmag BioTechnology Co., Ltd.). Therefore, comparing the RAST system against the commercial NA extractor is meaningful and valuable in terms of inspection performance. In this experiment, we used PBS to dissolve synthesized COVID-19 pseudo virus samples to simulate the virus detection environment. The final sample concentrations ranged from 10^3 copies/mL to 10^6 copies/mL, with a total solution volume of 100 μL (refer to Table S3 for experimental details). Fig. 5(E) demonstrates a strong linear relationship between the Ct values of PCR and the concentration of COVID-19 RNA using both the RAST system and the commercial NA extractor. However, the efficiency of COVID-19 RNA extraction using the RAST system is generally higher, as evidenced by the lower mean Ct values with the RAST system indicating greater extraction of COVID-19 RNA templates. Additionally, Fig. 5(E&F) illustrates that, as the concentration of COVID-19 RNA decreases, the advantage of the RAST in NA extraction becomes more pronounced. There are two main reasons for these results. Firstly, as previously mentioned, magnetic MBs tend to clump together when they are attracted by a strong magnetic field, which impacts RNA adsorption. In contrast, the dispersive effect of acoustic streaming exposes more adsorption sites of magnetic MBs in three-dimensional space, enhancing RNA capture. Secondly, due to the low concentration of COVID-19 RNA, a high-intensity mixing capability is necessary. And the RAST system at the D-SMR offers high-speed mixing in three-dimensional space, providing more opportunities for RNA molecules and magnetic MB adsorption sites to interact. For instance, with a PBS solution of 100 μL containing just 100 copies of COVID-19 RNA, the RAST system shows a mean Ct value approximately 0.64 lower than that of the commercial NA extractor, indicating a 1.56-fold increase in RNA template extraction efficiency with the RAST system. Therefore, we can assume that our RAST system can satisfy the extraction of low concentration NA samples and prevent the problem of false positives.

4. Conclusions

In this study, a portable nucleic acid extraction system based on the reconfigurable acoustic streaming tweezer (RAST) was successfully developed. By integrating two GHz solid-mounted thin-film piezoelectric resonators (SMRs) into a compact reaction chamber, flexible switching between the centrifuge-type particle separation (single SMR mode) and the vortex-type solution mixing (double SMR mode) was achieved, meeting the multi-step liquid handling requirements in the nucleic acid extraction process without complex peripherals. Compared to traditional magnetic bead – based nucleic acid extraction, which requires a centrifuge to prevent adhesion to the EP tube wall and a vortex mixer for bead dispersion, the RAST system stands out for its lack of such large, heavy external devices, offering greater portability and convenience. In terms of particle manipulation, the mechanisms of the acoustic radiation force (ARF) and the acoustic streaming force (ASF) on microbeads (MBs) under different powers were clarified. The optimal power for single SMR to capture MBs was determined to be 5.4 mW, and the suitable power for double SMR to mix MBs was 200 mW. The placement angle of the double SMR and the boundary dimensions of the reaction chamber were optimized through simulations and experiments to improve the mixing efficiency. In the nucleic acid extraction experiments, the system exhibited good performance when handling complex samples such as whole blood and serum. An 80 % nucleic acid recovery rate was achieved from rat whole blood, and the detection sensitivities for adenovirus DNA and COVID-19 RNA reached 10^2 IU/mL and 10^3 Copies/mL, respectively. Moreover, the sensitivity of the system was better than that of commercial nucleic acid extractors when handling small-volume samples. In summary, this system has significant advantages in achieving efficient and portable nucleic acid extraction and is expected to be widely used in the field of point-of-need testing (PONT) and other fields.

In this study, we focused on nucleic acid extraction from whole blood and serum, demonstrating the system's promising performance. Whole blood, a complex biological sample, already poses numerous challenges due to its intricate composition, making it a representative subject for our research. However, it's important to note that there are limitations to our current work. Future research could explore the impact of more complex samples, such as those with extremely high lipid or protein content, on the extraction efficiency and device performance to further expand the applicability of the developed nucleic acid extraction system. Besides, regarding for large volume sample or multiple samples handling, continuous flow injection processing or arraying of devices could be considered.

5. Data availability

Data will be made available on request.

CRediT authorship contribution statement

Tiechuan Li: Writing – review & editing, Writing – original draft, Validation, Software, Data curation, Conceptualization. **Rui You:** Writing – review & editing, Visualization, Software, Formal analysis, Conceptualization. **Xiaotian Shen:** Writing – original draft, Data curation, Conceptualization. **Zhiwei Li:** Software, Methodology. **Yang Yang:** Writing – review & editing, Methodology, Formal analysis. **Ziyu Han:** Writing – review & editing. **Xuexin Duan:** Writing – review & editing, Supervision, Project administration, Funding acquisition,

Formal analysis, Conceptualization.

Declaration of competing interest

The authors declare that they have no known competing financial interests or personal relationships that could have appeared to influence the work reported in this paper.

Acknowledgments

The authors gratefully the financial support from the National Natural Science Foundation of China (NSFC No. 62174119)

Appendix A. Supplementary data

Supplementary data to this article can be found online at https://doi.org/10.1016/j.ultsonch.2025.107404.

References

[1] M. Joshi, J.D. Deshpande, Polymerase chain reaction: methods, principles and application, Int. J. Biomed. Res. 2 (2011) 81–97.
[2] B. Udugama, P. Kadhiresan, H.N. Kozlowski, A. Malekjahani, M. Osborne, V.Y. C. Li, H. Chen, S. Mubareka, J.B. Gubbay, W.C.W. Chan, Diagnosing COVID-19: the disease and tools for detection, ACS Nano 14 (2020) 3822–3835.
[3] S.H. Lee, S.W. Kim, J.Y. Kang, C.H. Ahn, A polymer lab-on-a-chip for reverse transcription (RT)-PCR based point-of-care clinical diagnostics, Lab Chip 8 (2008) 2121–2127.
[4] J. Wu, R. Kodzius, K. Xiao, J. Qin, W. Wen, Fast detection of genetic information by an optimized PCR in an interchangeable chip, Biomed. Microdevices 14 (2012) 179–186.
[5] J.S. Lee, J.J. Ahn, S.J. Kim, S.Y. Yu, E.J. Koh, S.H. Kim, H.S. Sung, J.W. Huh, S. Y. Hwang, POCT detection of 14 respiratory viruses using multiplex RT-PCR, BioChip J. 15 (2021) 371–380.
[6] H. Zhang, F. Huang, G. Cai, Y. Li, J. Lin, Rapid and sensitive detection of Escherichia coli O157:H7 using coaxial channel-based DNA extraction and microfluidic PCR, J. Dairy Sci. 101 (2018) 9736–9746.
[7] D. Obino, M. Vassalli, A. Franceschi, A. Alessandrini, P. Facci, F. Viti, An overview on microfluidic systems for nucleic acids extraction from human raw samples, Sensors (Basel) 21 (2021).
[8] K.A. Hagan, J.M. Bienvenue, C.A. Moskaluk, J.P. Landers, Microchip-based solid-phase purification of RNA from biological samples, Anal. Chem. 80 (2008) 8453–8460.
[9] D. Chen, M. Mauk, X. Qiu, C. Liu, J. Kim, S. Ramprasad, S. Ongagna, W.R. Abrams, D. Malamud, P.L. Corstjens, H.H. Bau, An integrated, self-contained microfluidic cassette for isolation, amplification, and detection of nucleic acids, Biomed. Microdevices 12 (2010) 705–719.
[10] P. Liu, X. Li, S.A. Greenspoon, J.R. Scherer, R.A. Mathies, Integrated DNA purification, PCR, sample cleanup, and capillary electrophoresis microchip for forensic human identification, Lab Chip 11 (2011) 1041–1048.
[11] D. Le Roux, B.E. Root, J.A. Hickey, O.N. Scott, A. Tsuei, J. Li, D.J. Saul, L. Chassagne, J.P. Landers, P. de Mazancourt, An integrated sample-in-answer-out microfluidic chip for rapid human identification by STR analysis, Lab Chip 14 (2014) 4415–4425.
[12] K. Chan, S.C. Weaver, P.Y. Wong, S. Lie, E. Wang, M. Guerbois, S.P. Vayugundla, S. Wong, Rapid affordable and portable medium-throughput molecular device for Zika virus, Sci. Rep. 6 (2016) 38223.
[13] D. Helb, M. Jones, E. Story, C. Boehme, E. Wallace, K. Ho, J. Kop, M.R. Owens, R. Rodgers, P. Banada, H. Safi, R. Blakemore, N.T. Lan, E.C. Jones-Lopez, M. Levi, M. Burday, I. Ayakaka, R.D. Mugerwa, B. McMillan, E. Winn-Deen, L. Christel, P. Dailey, M.D. Perkins, D.H. Persing, D. Alland, Rapid detection of Mycobacterium tuberculosis and rifampin resistance by use of on-demand, near-patient technology, J. Clin. Microbiol. 48 (2010) 229–237.
[14] J.H. Wang, L. Cheng, C.H. Wang, W.S. Ling, S.W. Wang, G.B. Lee, An integrated chip capable of performing sample pretreatment and nucleic acid amplification for HIV-1 detection, Biosens. Bioelectron. 41 (2013) 484–491.
[15] H. Yang, Z. Chen, X. Cao, Z. Li, S. Stavrakis, J. Choo, A.J. deMello, P.D. Howes, N. He, A sample-in-digital-answer-out system for rapid detection and quantitation of infectious pathogens in bodily fluids, Anal. Bioanal. Chem. 410 (2018) 7019–7030.
[16] X. Zhang, X. Wu, R. Peng, D. Li, Electromagnetically controlled microfluidic chip for DNA extraction, Measurement 75 (2015) 23–28.
[17] Y. Lu, M. Zhang, H. Zhang, J. Huang, Z. Wang, Z. Yun, Y. Wang, W. Pang, X. Duan, H. Zhang, On-chip acoustic mixer integration of electro-microfluidics towards in-situ and efficient mixing in droplets, Microfluid. Nanofluid. 22 (2018).
[18] H. Wu, Z. Tang, R. You, S. Pan, W. Liu, H. Zhang, T. Li, Y. Yang, C. Sun, W. Pang, X. Duan, Manipulations of micro/nanoparticles using gigahertz acoustic streaming tweezers, Nanotechnol. Precis. Eng. 5 (2022).
[19] Y. Yang, W. Pang, H. Zhang, W. Cui, K. Jin, C. Sun, Y. Wang, L. Zhang, X. Ren, X. Duan, Manipulation of single cells via a stereo acoustic streaming tunnel (SteAST), Microsyst. Nanoeng. 8 (2022) 88.
[20] D. Ahmed, A. Ozcelik, N. Bojanala, N. Nama, A. Upadhyay, Y. Chen, W. Hanna-Rose, T.J. Huang, Rotational manipulation of single cells and organisms using acoustic waves, Nat. Commun. 7 (2016) 11085.
[21] J. Friend, L.Y. Yeo, Microscale acoustofluidics: Microfluidics driven via acoustics and ultrasonics, Rev. Mod. Phys. 83 (2011) 647–704.
[22] X. Guo, M. Sun, Y. Yang, H. Xu, J. Liu, S. He, Y. Wang, L. Xu, W. Pang, X. Duan, Controllable cell deformation using acoustic streaming for membrane permeability modulation, Adv Sci (weinh) 8 (2021) 2002489.
[23] A.J. Conde, I. Keraite, A.E. Ongaro, M. Kersaudy-Kerhoas, Versatile hybrid acoustic micromixer with demonstration of circulating cell-free DNA extraction from sub-ml plasma samples, Lab Chip 20 (2020) 741–748.
[24] I. Iranmanesh, M. Ohlin, H. Ramachandraiah, S. Ye, A. Russom, M. Wiklund, Acoustic micro-vortexing of fluids, particles and cells in disposable microfluidic chips, Biomed. Microdevices 18 (2016) 71.
[25] R.H. Liu, R. Lenigk, R.L. Druyor-Sanchez, J. Yang, P.J.A.C. Grodzinski, Hybridization Enhancement Using Cavitation Microstreaming 75 (2003) 1911–1917.
[26] P.H. Huang, Y. Xie, D. Ahmed, J. Rufo, N. Nama, Y. Chen, C.Y. Chan, T.J. Huang, An acoustofluidic micromixer based on oscillating sidewall sharp-edges, Lab Chip 13 (2013) 3847–3852.
[27] H. Bachman, C. Chen, J. Rufo, S. Zhao, S. Yang, Z. Tian, N. Nama, P.H. Huang, T. J. Huang, An acoustofluidic device for efficient mixing over a wide range of flow rates, Lab Chip 20 (2020) 1238–1248.
[28] H.V. Phan, M.B. Coskun, M. Sesen, G. Pandraud, A. Neild, T. Alan, Vibrating membrane with discontinuities for rapid and efficient microfluidic mixing, Lab Chip 15 (2015) 4206–4216.
[29] S. Orbay, A. Ozcelik, H. Bachman, T.J. Huang, Acoustic actuation of in situ fabricated artificial cilia, J. Micromech. Microeng. 28 (2018).
[30] W. Cui, H. Zhang, H. Zhang, Y. Yang, M. He, H. Qu, W. Pang, D. Zhang, X. Duan, Localized ultrahigh frequency acoustic fields induced micro-vortices for submilliseconds microfluidic mixing, Appl. Phys. Lett. 109 (2016).
[31] S. Pan, H. Zhang, W. Liu, Y. Wang, W. Pang, X. Duan, Biofouling removal and protein detection using a hypersonic resonator, ACS Sens 2 (2017) 1175–1183.
[32] S. Pan, T. Jeon, D.C. Luther, X. Duan, V.M. Rotello, Cytosolic delivery of functional proteins in vitro through tunable gigahertz acoustics, ACS Appl. Mater. Interfaces 12 (2020) 15823–15829.
[33] X. Shen, T. Li, Z. Wang, X. Ke, S. Shen, H. Cui, Y. Yang, W. Guo, C. Sun, X. Duan, Ultrafast mixing for high-throughput droplet microfluidics using GHz acoustic streaming, Chem. Eng. J. 477 (2023).
[34] X. Chen, T. Li, A novel passive micromixer designed by applying an optimization algorithm to the zigzag microchannel, Chem. Eng. J. 313 (2017) 1406–1414.